Characterizing critical behavior and band tails on the metal-insulator transition in structurally disordered two-dimensional semiconductors: Autocorrelation and multifractal analysis

Bong Gyu Shin [1,2] Ji-Hoon Park [3] Jing Kong [3] and Soon Jung Jung [1,*]
[1] Max Planck Institute for Solid State Research, Heisenbergstrasse 1, 70569 Stuttgart, Germany
[2] Department of Nano Science and Technology, SKKU Advanced Institute of Nanotechnology (SAINT), Sungkyunkwan University (SKKU), Suwon 16419, Republic of Korea
[3] Department of Electrical Engineering and Computer Science, Massachusetts Institute of Technology, Cambridge, Massachusetts 02139, USA

(Received 21 June 2023; revised 5 September 2023; accepted 11 September 2023; published 10 October 2023)

Our previous study observed the localization-delocalization transition and critical quantum fluctuations of the local density of states (LDOS) on the structurally disordered two-dimensional (2D) semiconductor MoS_2. This transition corresponds to the metal-insulator transition (MIT) reported in transport measurements. The structural disorder in MoS_2 caused curvature-induced band gap fluctuations, leading to charge localization and unusual band edge flattening through doping. The critical behavior for the MIT was analyzed using autocorrelation and multifractality of LDOS mapping results. However, the effect of structural disorder on critical points has not been fully explored. Here, we systematically investigated the impact of structural disorder on band tail formation and critical doping concentration by examining the radial-averaged autocorrelation and multifractality of LDOS in 2D semiconductors. Our finding indicates that the radial-averaged autocorrelation and multifractality of LDOS characterize the band tail ranges and band edge flattening in disordered 2D semiconductors. Decaying regions in the radial-averaged autocorrelation profile and first-order derivative of singularity peak positions determine band tail ranges. Increased structural disorder led to larger band tail widths near valence and conduction band edges, while the doping-induced band edge flattening altered band tail widths for each valence and conduction band. As the band edge is flattened due to doping, the LDOS map near the critical energy becomes uniform, exhibiting a divergence in the localization length. The average value of conduction and valence band tail widths remained almost constant regardless of doping control, serving as a representative value for the degree of structural disorder. For the MIT, we found that the critical doping concentration depends on the degree of structural disorder in 2D semiconductors. Our findings provide valuable insights into the fundamental physics of structurally disordered 2D semiconductors in relevance to quantum phase transitions, which could have important implications for designing and optimizing electronic/optoelectronic devices based on 2D materials.

DOI: 10.1103/PhysRevResearch.5.043029

I. INTRODUCTION

The metal-insulator transition (MIT) in a disordered two-dimensional (2D) system remains an enigma among the quantum phase transitions, involving the fundamental challenges of comprehending the order parameter and dynamical nature [1,2]. The disorder-driven quantum phase transitions (including disorder-induced MITs) exhibit a critical point (critical doping concentration for MIT) that separates localized (insulating) and delocalized (conducting) states. In the noninteracting picture, the disorder-driven MIT is often called Anderson transitions [1–4]. The one-parameter scaling theory of localization in disordered 2D systems at zero temperature (for Wigner-Dyson orthogonal symmetry class AI) predicted only localized states, not allowing the MIT [5], but the existence of a 2D MIT has been reported in 2D electron systems of Si metal-oxide field-effect transistors and other 2D semiconductors [6–11]. To find a universal theory for the 2D MIT, many aspects of Anderson transitions have been investigated in terms of symmetry classes [1–3]. As it turns out, many symmetry classes allow MIT or critical behaviors in 2D systems [3]. On the other hand, the field theoretical approach with the nonlinear sigma model has been developed, and interactions in a system have been proven to provide vital roles for the MIT [1–3,12–14]. To understand the criticality of the MIT, two-point correlations and multifractal analysis of the local density of states (LDOS) have been proposed to characterize the quantum critical phenomena [1–3,15–17]. The distribution of LDOS or the amplitude of wave functions at an energy level is closely related to the order parameter function of the Anderson transitions [3,18].

The localization-delocalization transition with criticality in 2D semiconductors was directly observed, revealing the general mechanism of structural-disorder-driven critical quantum fluctuations of wave functions, charge localization, and band tails along with the doping-induced band edge flattening [19]. Structural disorder in 2D semiconductors induces band gap fluctuations that act like random potentials, leading to charge localization that forms band tails near the band edges. As the doping level increases, the local band bending, resulting from

*s.jung@fkf.mpg.de

Published by the American Physical Society under the terms of the Creative Commons Attribution 4.0 International license. Further distribution of this work must maintain attribution to the author(s) and the published article's title, journal citation, and DOI. Open access publication funded by the Max Planck Society.

the localized charge, generates an unusually uniform state above the critical energy. This was verified through the radial-averaged autocorrelation, singularity spectra, and normalized distribution of LDOS, which were extracted from scanning tunneling spectroscopy (STS) results. With the band edge flattening through doping, a dramatic localization-delocalization transition occurred from fluctuating (disorder, localized) to homogeneous (order, extended) states. This transition corresponds to the MIT in 2D semiconductors [19].

During the localization-delocalization transition, structural disorder plays a crucial role in enabling the transition to take place. As such, it is essential to understand the quantitative relationship between the critical doping concentration (or critical energy) and the strength of structural disorder. Through the microscopic mechanism of the MIT, the critical doping concentration at which the MIT occurs can be expected to depend on the degree of structural disorder. However, the quantitative relation between critical doping concentration (or critical energy) and the strength of structural disorder has not been fully investigated. The radial-averaged autocorrelation profile of disordered 2D semiconductors has also not yet been fully explored for the structural disorder of varying strength.

In this study, we investigate the relation between the strength of structural disorder and the MIT by analyzing the radial-averaged autocorrelation and multifractality of LDOS. The radial-averaged autocorrelation profile and peak positions (α_0) within singularity spectra for a specific structural disorder demonstrate critical behavior, as well as the emergence of band tails and band edge flattening through doping. We demonstrate that the first derivatives of α_0 of LDOS maps as a function of energy precisely determine energy intervals of band tails. When reaching the critical energy, the localization length becomes divergent as the band edge flattening approaches its limit. The relation between the critical doping concentration and the spatial average of absolute bending strain was calculated to demonstrate how the critical doping concentration depends on the strength of the structural disorder. Our finding indicates that when the structural disorder is more pronounced, the critical doping concentration becomes higher due to the larger capacity of the localized states. An ideal flat case does not display any localized states due to its zero curvature, which means there is no MIT. Then, the intrinsic carrier concentration in the flat case is assigned as the critical doping concentration. The effective critical doping concentration at finite temperatures is lower than that at 0 K, as the thermal excitation of carriers aids percolation-type conductivity [11]. The critical behavior determined using autocorrelation and multifractality calculated from the tight-binding method was found to be consistent with the experimental results of autocorrelation and multifractality analyzed from STS results.

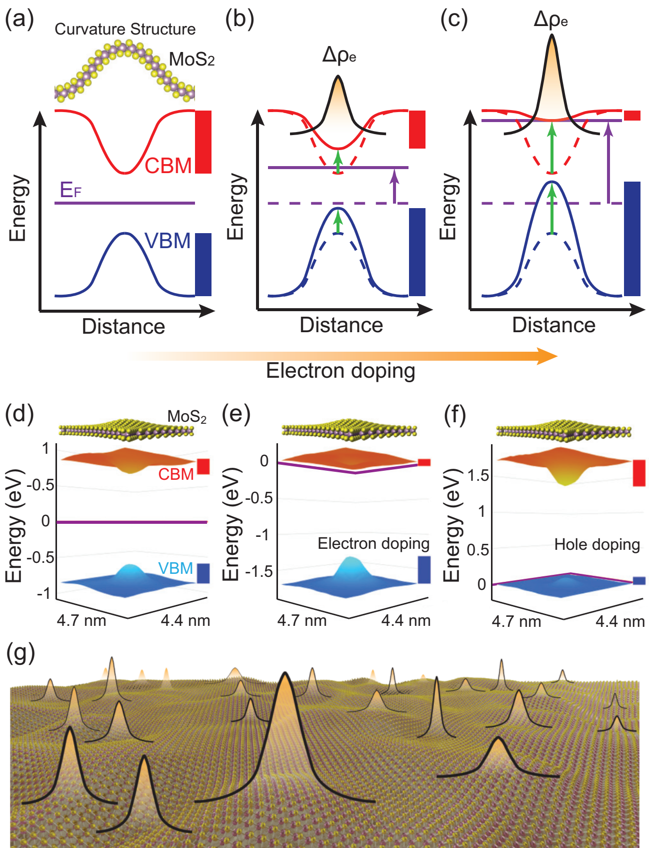

FIG. 1. Curvature-induced band gap fluctuations and charge localization mechanism in structurally disordered monolayer MoS_2. [(a)–(c)] Schematic illustrations of curvature-induced band gap fluctuations in monolayer MoS_2, and charge localization with doping control ($\Delta\rho_e$ represents electron doping charge density). Curvature in deformed 2D semiconductors causes band gap reduction (a), and a doping charge localized at the curvature region [(b), (c)]. This localized charge leads to local band bending, and band edge flattening occurs as the doping level increases [(b), (c)]. Each dashed line represents the neutral state of (a). Green and purple arrows indicate the band edge flattening and the Fermi level (E_F) changes by doping, respectively. [(d)–(f)] DFT calculation results for neutral (d), electron-doped (e), and hole-doped (f) cases in a spherical bending of MoS_2 (inset at the top). The curvature region in the deformed MoS_2 shows band gap reduction. High electron- (hole-) doping results in conduction (valence) band edge flattening [(e), (f)]. Each plot's red (blue) bar indicates CBM (VBM) fluctuation ranges. Purple lines indicate the Fermi level for each plot [for [(e), (f)], doping concentration $\sim 7.09 \times 10^{13}$ cm^{-2}). (g) A cartoon illustrating charge localization in the structurally disordered MoS_2. Curvature-induced band edge (gap) fluctuations in structurally disordered MoS_2 function like a random potential for doping charges, analogous to the Anderson transitions. Charge localizations are illustrated by lines with shaded areas. Yellow and purple spheres represent S and Mo atoms, respectively.

II. STRUCTURAL-DISORDER-DRIVEN LOCALIZATION-DELOCALIZATION TRANSITION

A. Curvature-induced charge localization

Curvature formation in 2D semiconductor MoS_2 on a substrate leads to band gap fluctuations, which were directly observed in atomic resolution scanning tunneling microscopy (STM) and STS images in previous studies [19,20]. By conforming to the substrate's surface roughness, the curvature appeared randomly as bending strain. Bending energy is lower than the adhesion energy of 2D monolayers, making bending naturally easy [21,22]. Figures 1(a)–1(c) illustrate the

mechanism of curvature-induced band gap (edge) fluctuations and charge localization. The high curvature region displays a significant band gap reduction of up to ∼1 eV [Fig. 1(a)] [20]. When electron doping is applied, the doping charge prefers to localize in lower band gap (or edge) regions [Fig. 1(b)] [19]. The localized electron (hole) charge induces local band bending due to Coulomb interactions, leading to an unusual flattening of the conduction (valence) band edge [Fig. 1(c)]. The main reason for this significant band edge flattening is the strong Coulomb interactions among charge carriers, as 2D monolayers have a small volume with atomic-scale thickness that offers less screening for Coulomb interactions [23]. Mapping results of STS revealed the band edge flattening due to doping [19]. For electron doping, the fluctuation range of the conduction (valence) band edge narrows (widens) [Fig. 1(c)]. For hole doping, valence band edge flattening occurs, and doping-induced changes in fluctuations of band edges reverse compared to the trends in electron doping cases. Density functional theory (DFT) calculations quantitatively predict curvature-induced band gap fluctuation and band edge flattening through doping [Figs. 1(d)–1(f)]. For a spherical bending of monolayer MoS_2, DFT calculations demonstrate band gap reduction in the curvature region [Fig. 1(d)] and doping-induced band edge flattening (for electron (hole) doping, Fig. 1(e) [Fig. 1(f)]). It is known that bending strain in 2D semiconductors results in band gap fluctuations. When doping is introduced, the equilibrium of the electrochemical potential, establishing the Fermi level, involves the flattening of the band edge (local band bending) through doping due to the strong Coulomb interactions less screened by 2D semiconductors [19].

In monolayer MoS_2 with structural disorder, curvature-induced band gap (edge) fluctuations act like random potentials for doping charge, analogous to the Anderson transition [4,19]. Figure 1(g) presents a cartoon depicting a random distribution of localized doping charge over curvatures in a structurally disordered MoS_2. The microscopic origin of MIT was confirmed in a previous study using STM and STS at the atomic scale [19]. The revealed mechanism showed that local band bending by localized charge led to an unusual band edge flattening due to the strong Coulomb interaction. The localization-delocalization transition of LDOS at the critical energy, along with the band edge flattening through doping, was observed, and the criticality was analyzed using autocorrelation and multifractality of STS mapping results [19]. The random distribution of localized states was also confirmed to form the exponential band tails near the band edges [19]. The microscopic mechanism of MIT was found to be generally applicable to a wide variety of 2D semiconductors.

B. Autocorrelation analysis

The STM image of neutral MoS_2 on SiO_2 [Fig. 2(a)] revealed structural disorder due to the surface roughness of the SiO_2 substrate. Near the conduction band minimum (CBM) at 0.75 eV, charge localization was observed in the STS map as shown in Fig. 2(b). At a higher energy level of 2.0 eV above CBM, state fluctuations extended over the whole area [Fig. 2(c)], and complexity associated with structural disorder remains. The radial-averaged autocorrelation profile of MoS_2 on SiO_2 [Fig. 2(d)] presents rapidly decaying regions near band edges, corresponding to disordered localized states that formed band tail regions. Stronger structural disorder in MoS_2 exhibits more rapidly decaying regions due to the stronger charge localization.

For MoS_2 on highly oriented pyrolytic graphite (HOPG) [Fig. 2(e)], distinct charge localization was not observed near CBM (1.6 eV) [Fig. 2(f)] due to the weak structural disorder. At the higher energy level of 2.2 eV above CBM, the STS map [Fig. 2(g)] also exhibited uniform LDOS due to the weak structural disorder. The radial-averaged autocorrelation profile of MoS_2 on HOPG [Fig. 2(h)] shows an almost constant value along the radial distance at the allowed energy levels, indicating the uniformity of LDOS as shown in Figs. 2(f) and 2(g). The energy range of rapidly decaying behaviors near the band edges in Fig. 2(h) is narrow due to weak structural disorder in MoS_2 on HOPG, which indicates narrow band tails. Radial-averaged autocorrelation profiles characterize the band tails of localized states under varying structural disorder strengths, from weak to strong cases.

The strongly localized states show a rapidly decaying amplitude of the wave function, $|\psi(\boldsymbol{r})|^2 \sim \exp(-|\boldsymbol{r}|/\xi_L)$, where $|\boldsymbol{r}|$ is the distance from the center of the localized states and ξ_L is the localization length that is smaller than the (effective) system size [3]. If wave functions are extended, the characteristic width of the wave functions becomes larger (ideally infinite) than the (effective) system size. Localization in wave functions (ψ) can be measured by the radial-averaged autocorrelation $C(|\boldsymbol{R}|)$ which is defined by $\langle|\psi(\boldsymbol{r},E)|^2|\psi(\boldsymbol{r}+\boldsymbol{R},E)|^2\rangle$ or $\langle\rho(\boldsymbol{r},E)\rho(\boldsymbol{r}+\boldsymbol{R},E)\rangle$, where ρ is LDOS proportional to $|\psi(\boldsymbol{r},\ E)|^2$, $|\boldsymbol{R}|$ is a radial distance, and $\langle\cdot\rangle$ means an average over the disorder [16]. Near the critical point of the localized-delocalized transition of the wave functions, $C(|\boldsymbol{R}|)$ is proportional to $(|\boldsymbol{R}|/L)^{-\eta}(l<|\boldsymbol{R}|<L)$, where η is the critical exponent, l is the length scale of the elastic mean free path, and L is the effective system size, $L = \min\{L_\phi, \xi_c, L_s\}$ (L_ϕ: dephasing length; ξ_c: correlation length; and L_s: system size) and satisfying that $\eta = -\Delta_2$, where Δ_2 is the anomalous multifractal exponent of moment $q = 2$ [16]. Such a power law behavior of $|\boldsymbol{R}|^{-\eta}$ indicates the absence of length scales, which makes a continuous connection between localized (finite, disorder) and delocalized (ideally infinite, order) states [24]. The power law behavior is relevant to the critical quantum fluctuation that must be compatible with localization and delocalization regions, requiring scale invariance (the absence of length scale) associated with multifractality. The fractality of a system refers to self-similarity, regardless of the scale of the system (the absence of length scale). Multifractality means that a system has many parts with different fractalities.

Using the tight-binding approach with the three-band model over the third-nearest neighbor [25], the curvature-induced band gap fluctuations and formation of band tails were fully investigated for various strengths of structural disorders and doping concentrations.

Figure 2(i) shows horizontal stacking of dI/dV spectra at each spatial point extracted by STS mapping in which the blue-colored region corresponds to the band gap. The observed band gap fluctuations were highly correlated with the mean curvature in the monolayer

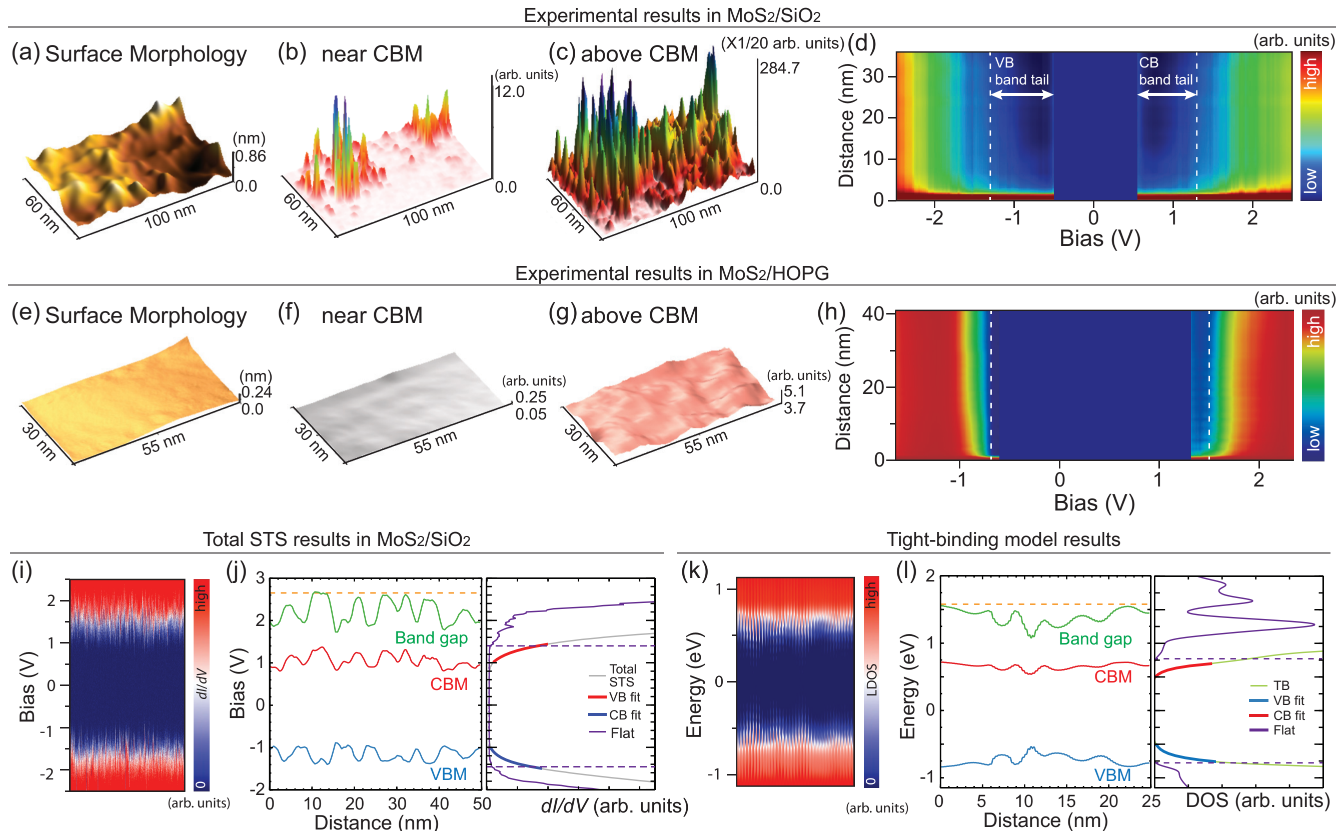

FIG. 2. Direct observation of localized states and characterization of band tails in structurally disordered monolayer MoS_2. [(a)–(d)] STM topography of MoS_2 on SiO_2 (a), STS maps near CBM (0.75 eV) (b) and above CBM (2 eV) (c), and radial-averaged autocorrelation profile (d). The structural disorder in MoS_2 on SiO_2 leads to strong charge localization near the band edge (b), characterized by a decaying region in the radial-averaged autocorrelation. The band tails consist of localized states. [(e)–(h)] STM topography of MoS_2 on HOPG (e), STS maps near CBM (1.61 eV) (f) and above CBM (2.2 eV) (g), and radial-averaged autocorrelation profile (h). Charge localization is negligible in the weak structure disorder from the flat HOPG (f). (i) Horizontally stacked STS results (dI/dVs) from each position. (j) Typical line profiles for local VBM, CBM, and band gap along a straight line in the real space extracted from the STS results. The side inset shows DOS extracted from STS results (gray line), revealing exponential band tails near band edges. (k) Horizontally stacked calculated LDOS results using the tight-binding (TB) method with structural disorder. (l) Typical line profiles for local VBM, CBM, and band gap extracted from the calculated LDOS using TB methods. The side inset shows the calculated DOS results (light green line) with exponential band tails near band edges. TB modeling results align well with the experimental results [(i), (j)]. The blue, red, and purple curves in each DOS plot are fitting lines for valence (blue) and conduction (red) band tails, and reference of DOS (purple) in a flat case. The dashed purple lines in each DOS plot indicate the band edges for flat cases. Band gap fluctuations are denoted by a blue-colored region [(i), (k)]. The Fermi level is set to zero.

MoS_2 [20]. Figure 2(j) shows the typical fluctuations of local CBM, VBM, and band gap along a spatial straight line. The right-side inset in Fig. 2(j) shows the density of states (DOS, gray line) extracted from the STS results with exponential fitting lines for band tails of valence (blue line) and conduction (red line) band edges exhibiting the characteristic band tail width (φ) of ~0.2 eV by $\exp(-|E|/\varphi)$, where E is the energy of the electrons. The DOS for the flat region in MoS_2 [purple line in Fig. 2(j)] exhibited the intrinsic band gap size of 2.65 eV on SiO_2 substrate [20]. The exponential shapes of the band tails are expected to be only formed by the randomness of structural disorder [26].

For the theoretical results in structural disorder, the structural modeling for disordered MoS_2 was constructed with the tight-binding method [19,25]. To mimic the surface fluctuation observed in STM results of MoS_2 on SiO_2, random deformation of MoS_2 was generated by a collection of random Gaussian bumps with tuning parameters. The tight-binding calculations for the disordered MoS_2 model show random band gap fluctuations [Fig. 2(k)] as observed in the experimental results [Fig. 2(i)]. The calculated typical line profiles for CBM, VBM, and the band gap along a spatial straight line [Fig. 2(l)] align well with the experimental results in disordered MoS_2 on SiO_2. The right-side inset in Fig. 2(l) shows the calculated DOS results for the disordered MoS_2 (light green line) with exponential band tails near the band edges (red and blue fitting lines) and for flat MoS_2 (purple line). The tight-binding approach fully reconstructed the observed structural disorder effect with the mechanism of curvature-induced band gap fluctuations as explained in the previous study [19,20].

To understand the formation of the band tails under structural disorder, scaling of structural disorder was conducted to evaluate the radial-averaged autocorrelation profiles under the effects of various disorder strengths (Fig. 3). The left-side insets in Fig. 3 show random fluctuations of surface

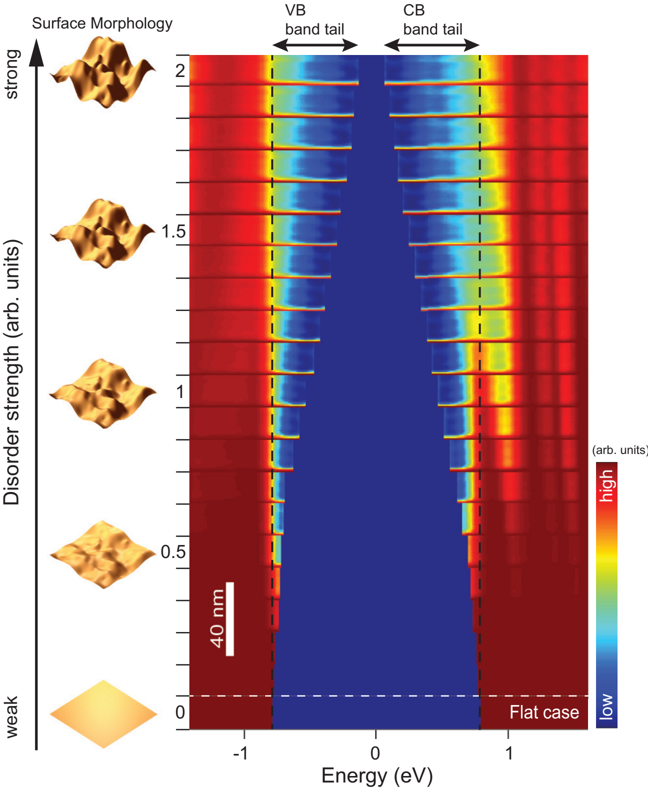

FIG. 3. Effect of structural disorder on band tail formation. The radial-averaged autocorrelation profiles for each structural disorder strength (stacked vertically) show changes in band tail ranges, which were extracted from the tight-binding calculations. The fluctuation range of surface morphology was scaled, representing structural disorder strength from weak to strong disorder as shown in the insets on the left side. The rapid decay regions in the radial-averaged autocorrelation profiles correspond to the band tail regions. The flat 0 case at the bottom shows constant radial-averaged autocorrelation, corresponding to the uniform LDOS distribution without disorder. The blue-colored regions in autocorrelation profiles correspond to the band gap regions, which are forbidden. The vertical dashed black lines indicate band edges for the flat case.

morphologies with different strengths of structural disorder. Larger height fluctuations allow larger absolute curvatures leading to significant changes in band gap. As disorder strength increases, band tail widths near band edges become larger. Typically, the reported characteristic width of the band tail in MoS_2 on SiO_2 was ~0.1 eV [27], corresponding to near the "1" case of disorder strength in Fig. 3, displaying a similar surface roughness range of MoS_2 on SiO_2. The theoretical results align well with the experimental results of MoS_2 on both SiO_2 and HOPG cases, revealing the continuous changes of band tails as a function of structural disorder strength.

C. Doping-induced band edge flattening

When doping is applied to structurally disordered MoS_2, the band edge flattening occurs due to the strong Coulomb interaction which is less screened by the thin material itself [19,23]. For electron (hole) doping, the conduction (valence) band edge is flattened by the local band bending of the localized charge until reaching the equilibrium of electrochemical potential (determination of the Fermi level) [19]. The doping-induced band edge flattening effects were calculated using the tight-binding results. Figure 4(a) shows electron-doping charge localization with the flattening of the conduction band edge. The localized doping-charge density [$\Delta\rho_e$ in Fig. 4(a)] for case 1 in Fig. 3 becomes large by accumulation of doping charge towards the local minimums of the curvature-induced potentials when the doping concentration increases [from bottom 0 (neutral) to top 5 in Fig. 4(a)]. For each doping level for case 1 in Fig. 3, the radial-averaged autocorrelation profiles of LDOS [Fig. 4(b)] shows narrowing of the rapidly decaying region near the conduction band edge and widening of the rapidly decaying region near the valence band edge, corresponding to the conduction band edge flattening via doping. The highest doping level case, 5, in Fig. 4(b) corresponds to the almost perfect flattening of the conduction band edge. For the flattening limit, the band tail near the conduction band edge vanishes. At the flattening limit, the radial-averaged autocorrelation profiles above the conduction band edge hardly changed along the radial distance due to the uniformity of LDOS caused by the band edge flattening. Figure 4(c) shows the total radial-averaged autocorrelation profiles at the flattening limit as a function of structural disorder strength, as in Fig. 3. The band tail near the valence band edge elongates further when the structural disorder becomes strong. Due to the flattening of the conduction band edges through doping, the range of the band tail near the valence band edge is almost twice as wide as in the neutral case, as shown in Fig. 3.

In Fig. 4(d), the experimental result of the radial-averaged autocorrelation profile from electron-doped MoS_2 on SiO_2 (doping concentration ~5.7×10^{12} cm^{-2}) exhibited a narrow decaying region near the conduction band edge, corresponding to the flattening of the conduction band edge, which is in good agreement with case 2 in Fig. 4(b). Above the critical energy or band tail region, the flattening of the conduction band edge through high doping led to the spatially uniform extended states, regardless of the structural disorder, which was not observed from the neutral case as in Fig. 2(c) [19]. Truly 2D uniform states appeared as they passed through the localization-delocalization transition, exhibiting almost constant values of the radial-averaged autocorrelations due to the doping-induced band edge flattening.

In Fig. 5(a), the calculated DOS by the tight-binding method for the doping cases in Figs. 4(a) and 4(b) shows the conduction band edge flattening and widening of the band tail near the valence band edge. The DOS near the band edges for each doping level exhibited exponential band tails and the linearity of the exponential band tails in log plots characterized the width of band tail (φ) by fitting of $\exp(-|E|/\varphi)$ as shown in Figs. 5(b) (valence band) and 5(c) (conduction band). The characteristic widths of band tails ($\varphi_{\mathrm{CB\ or\ VB}}$ for conduction or valence band) were plotted in Fig. 5(d). The average values (φ_{avg}) of the band tails of the conduction and valence bands remain almost constant, representing a value that is independent on doping control. The band tail width ($\varphi_{\mathrm{CB\ or\ VB}}$) results are in good agreement with the radial-averaged autocorrelation results [Fig. 4(b)].

It is important to note that when hole doping is applied, the changes in band tails through electron doping are

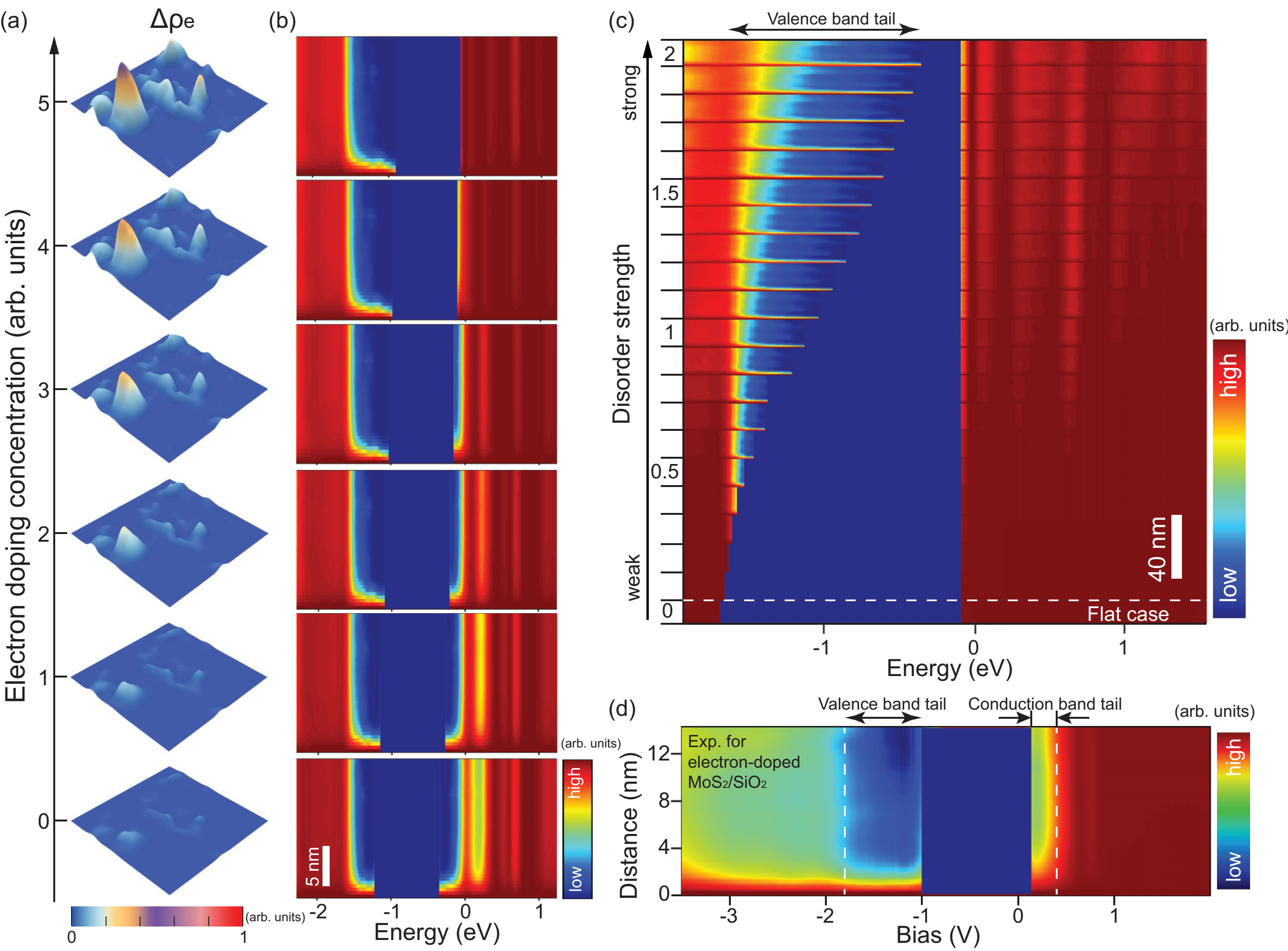

FIG. 4. Band edge flattening through doping in structural disorder. (a) Tight-binding method calculation results for doping charge densities ($\Delta\rho_e$) with electron-doping control (indexed from 0 to 5) in disordered MoS_2. The doping charge is localized under the curvature-induced band gap fluctuations. The larger index number indicates a higher doping concentration. The 0 means neutral states. (b) The radial-averaged autocorrelation profiles with doping control in disordered MoS_2 corresponding to (a). Higher electron doping concentration induces the flattening of the conduction band edge with the enlargement of the valence band tail width, showing decay along the radial distance (vertical direction; see the vertical scale bar at the bottom) in the autocorrelation. (c) Total radial-averaged autocorrelation profiles for various disorder strengths with conduction band edge flattening. The variation of disorder strength is the same as that in Fig. 3. Decaying regions near VBM in the autocorrelation profiles correspond to each band tail range. (For example, the arrow at the top indicates the band tail range for disorder strength 2.) (d) The radial-averaged autocorrelation profile of experimental results in electron-doped MoS_2/SiO_2 (doping concentration $\sim 5.7 \times 10^{12}$ cm^{-2}). Conduction band edge flattening was observed in good agreement with case 3 in (b). The blue-colored regions in autocorrelation profiles are band gap regions, which are forbidden.

reversed between the valence and conduction band sides (Figs. 7 and 8).

D. Multifractal analysis

To better understand band tails and criticality, we conducted a multifractal analysis of LDOS in the presence of structural disorder. We found that the LDOS's multifractality at various energy levels quantifies the band tail ranges connected to the critical energy of the localization-delocalization transition.

In Figs. 6(a)–6(d), the peak positions (α_0) of singularity spectra [$f(\alpha)$] satisfying $f(\alpha_0) = 2$ were extracted from the spatial fluctuations of LDOS as a function of energy (red lines). The absolute values of α_0 derivatives ($|d\alpha_0/dE|$) display peaks that characterize the band tail ranges on the energy axis [blue lines in Figs. 6(a)–6(d)]. For the MoS_2 on HOPG with weak structural disorder due to the HOPG's flatness, peaks of $|d\alpha_0/dE|$ characterized the narrow band tail ranges as shown in Fig. 6(a) (shaded region). In MoS_2 on SiO_2 with strong structural disorder, peaks of $|d\alpha_0/dE|$ characterize large band tail ranges [shaded areas in Fig. 6(b)]. With a higher doping level in MoS_2 on SiO_2 [as in Fig. 4(d)], peaks of $|d\alpha_0/dE|$ describe the band tails exhibiting the narrow (large) band tail range at the conduction (valence) band side, as expected by doping-induced band edge flattening [Fig. 6(c)]. All the multifractal analysis of the experimental results [Figs. 6(a)–6(c)] are in good

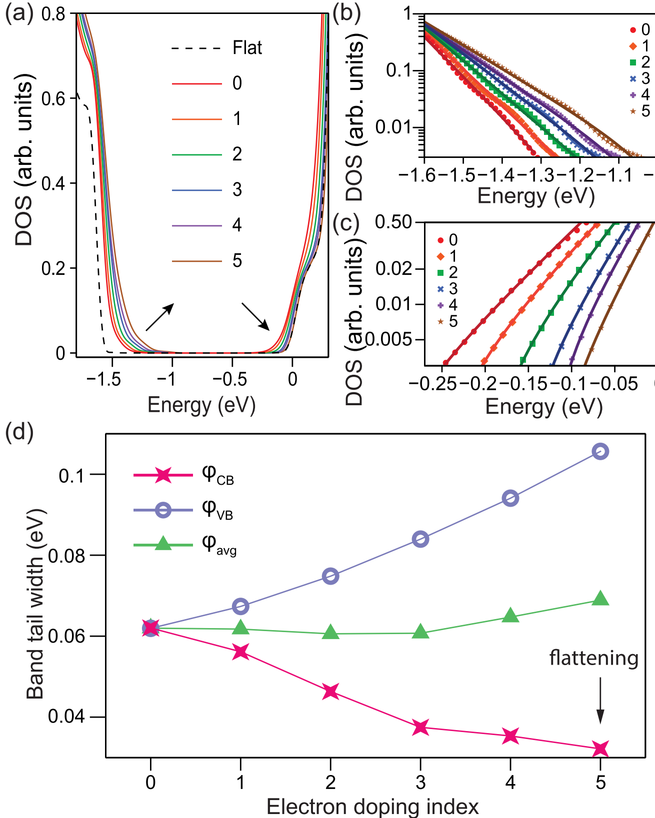

FIG. 5. Exponential band tails and band tail widths under doping control. (a) DOS profiles corresponding to Fig. 4(a). Higher doping concentration results in the extension of the valence band tail with flattening of the conduction band edge, close to that of the intrinsic flat MoS_2. [(b), (c)] Close-up log plots for the valence and conduction band edges from (a). Linearity in the log plots means the exponential behaviors of band tails. (d) Characteristic band tail widths extracted from DOS results (a). Flattening of conduction band edges leads to a diminishing conduction band tail width (φ_{CB}) via electron doping. The average values (φ_{avg}) of conduction and valence band tail (φ_{VB}) widths remain almost constant, representing a value that is not dependent on the doping level.

agreement with the autocorrelation profile results [Figs. 2(d), 2(h), and 4(d)].

The band edge flattening trends through doping were systematically investigated using multifractal analysis of the tight-binding results [Fig. 6(d)]. For a specific structural disorder (as in case 1 of Fig. 3), the multifractality results demonstrate that the conduction (valence) band tail range (shaded regions) narrows (widens) with the flattening of the conduction band edge as electron doping increases [as in Fig. 4(b)]. The band tail ranges through doping are plotted for conduction and valence band sides in Fig. 6(e). The average (ΔE_{avg}) of the valence and conduction band tail ranges (ΔE_{VB} and ΔE_{CB}) is nearly constant, similar to the average (φ_{avg}) of the characteristic band tail widths for valence and conduction bands [Fig. 5(d)]. It is noteworthy to mention that when hole doping is applied, the changes in Fig. 6(d) by electron doping are reversed between the valence and conduction band sides. In addition, we observed that amplitudes of α_0 values at the limit of the band edge flattening could be heavily influenced by the mean value of the absolute bending strain across a region, as depicted in Fig. 9. When considering the amplitude of α_0, it becomes apparent that further research is necessary to understand the interplay of the Coulomb interactions among charges, particularly at elevated doping concentrations.

Through multifractal analysis, we can accurately determine the energy intervals of band tails, which are unattainable when solely relying on the characteristic band tail width derived from the exponential fitting of DOS.

E. Criticality and localization length

In Fig. 6(f), the localization lengths characterized by the radial-averaged autocorrelation profiles of tight-binding results display divergence at the band edge flattening limit through high doping (case 5), corresponding to the critical behavior of the localization-delocalization transition. The localization lengths in cases from 0 (neutral) to 3 show small values near 5 nm in the band tail regions, indicating strong localization, which is consistent with the STM and STS and transport results [28].

It is worth noting that the critical exponent $\nu = 2.74$, estimated from case 5 of Fig. 6(f) using the fitting of $\sim |E - E_C|^{-\nu}$, is nearly identical to the reported values in the symplectic symmetry class of the Anderson transitions [29–31]. The tight-binding model used in this work neglects the effect of spin-orbit coupling (SOC). However, random strain causes fluctuations in hopping parameters and the doping-induced band edge flattening leads to random changes in on-site energy terms. The tight-binding models in symplectic cases included random changes in both hopping and on-site energy parameters, which is why the critical exponent could be close to the symplectic cases. The previous experimental results [19], however, reported a larger critical exponent than that of the symplectic class. The primary difference between our modeling and the previous experimental results involves two factors, Coulomb interactions among carriers and curvature-induced SOC changes. In particular, curvature-induced SOC changes in monolayer MoS_2 create an emergent gauge as a pseudomagnetic field [32], and the intrinsic magnetizations reported in previous experimental results [33,34] align well with the curvature-induced pseudomagnetic field and DFT calculations [19]. The pseudomagnetic field allows for a higher critical exponent value than that in the symplectic case [35], which is consistent with experimental results. We leave the pseudomagnetic field effects on the critical exponent for future works. However, the main conclusions in this work remain unaffected by the SOC effects.

Figure 6(g) displays the calculated LDOS maps for each doping case near the critical energy [$\sim$0 eV in Fig. 6(d)]. At the limit of the band edge flattening through doping, the uniformly extended state near the critical energy [case 5 in Fig. 6(g)] exhibited divergence of the localization length as a critical behavior [case 5 in Fig. 6(f)]. The singularity spectra of each LDOS map [Fig. 6(g)] are shown in Fig. 6(h), and the case 5 in Fig. 6(g) reveals monofractality towards the metallic limit (ideally, a function such that $f(\alpha = 2) = 2$, otherwise negative infinity [3]) due to band edge flattening through doping, which agrees well with the previous experimental results [19].

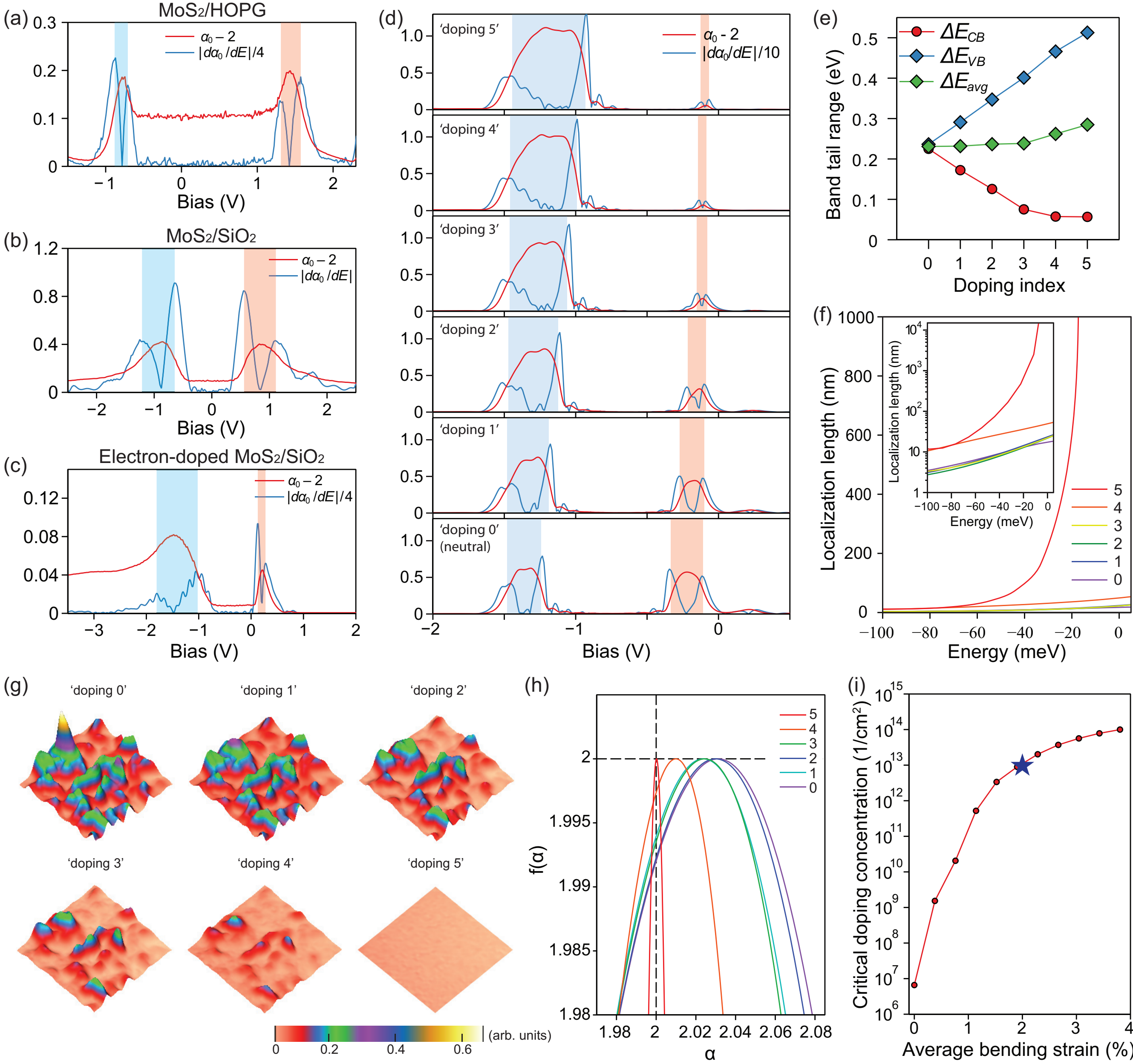

FIG. 6. Band tail characterization by multifractality of the local density of states. [(a)–(c)] Peak positions (α_0) of singularity spectra [such that $f(\alpha = \alpha_0) = 2$] from the spatial distributions of LDOS at given energies in MoS_2 on HOPG (a) [from Fig. 2(h)], MoS_2 on SiO_2 (b) [from Fig. 2(g)], and electron-doped MoS_2 on SiO_2 (c) [from Fig. 3(g)]. Absolute values of derivatives of the peak positions ($|d\alpha_0/dE|$) characterize the range of band tails, indicated by shaded areas (blue for valence band and red for conduction band). MoS_2 on HOPG is flatter than that on SiO_2, leading to the narrower band tail widths near the band edge. With a high electron doping in (c), the derivatives of α_0 show the narrowing of the conduction band tail and the widening of the valence band tail by flattening of band edges through the doping. (d) Tight-binding results for α_0 and derivatives of α_0 for various doping levels [corresponding to 0–5 as shown in Fig. 4(a)] from LDOS in the given structurally disordered MoS_2. The flattening of band edges by higher electron doping exhibits the narrowing of the conduction band tail and widening of the valence band tail in good agreement with the experimental results in [(b), (c)]. (e) Band tail ranges in each case of (d) were plotted. As electron doping increases (from 0 to 5), the conduction (valence) band tail range ΔE_{CB} (ΔE_{VB}) decreases (increases). The average (ΔE_{avg}) of the band tail ranges is nearly constant. (f) Localization lengths characterized in the radial-averaged autocorrelations show divergence as a critical behavior along with the full flattening of the band edge in doping case 5, where the conduction band tail range shrank and emerged into the critical energy, leading to the criticality. The inset is the log-scale plot of the localization lengths. The zero energy is set close to the critical energies of each case. (g) LDOS maps for each doping case near the critical energy (0 eV). The relative intensities of the maps are on the same scale. (h) Singularity spectra of LDOS maps in (g). (i) Critical doping concentration as a function of the average of absolute bending strain from variation in the strength of structural disorder. The flat case (0%) corresponds to the intrinsic doping concentration at 1 K. The blue star indicates the experimental result on the SiO_2 substrate [9].

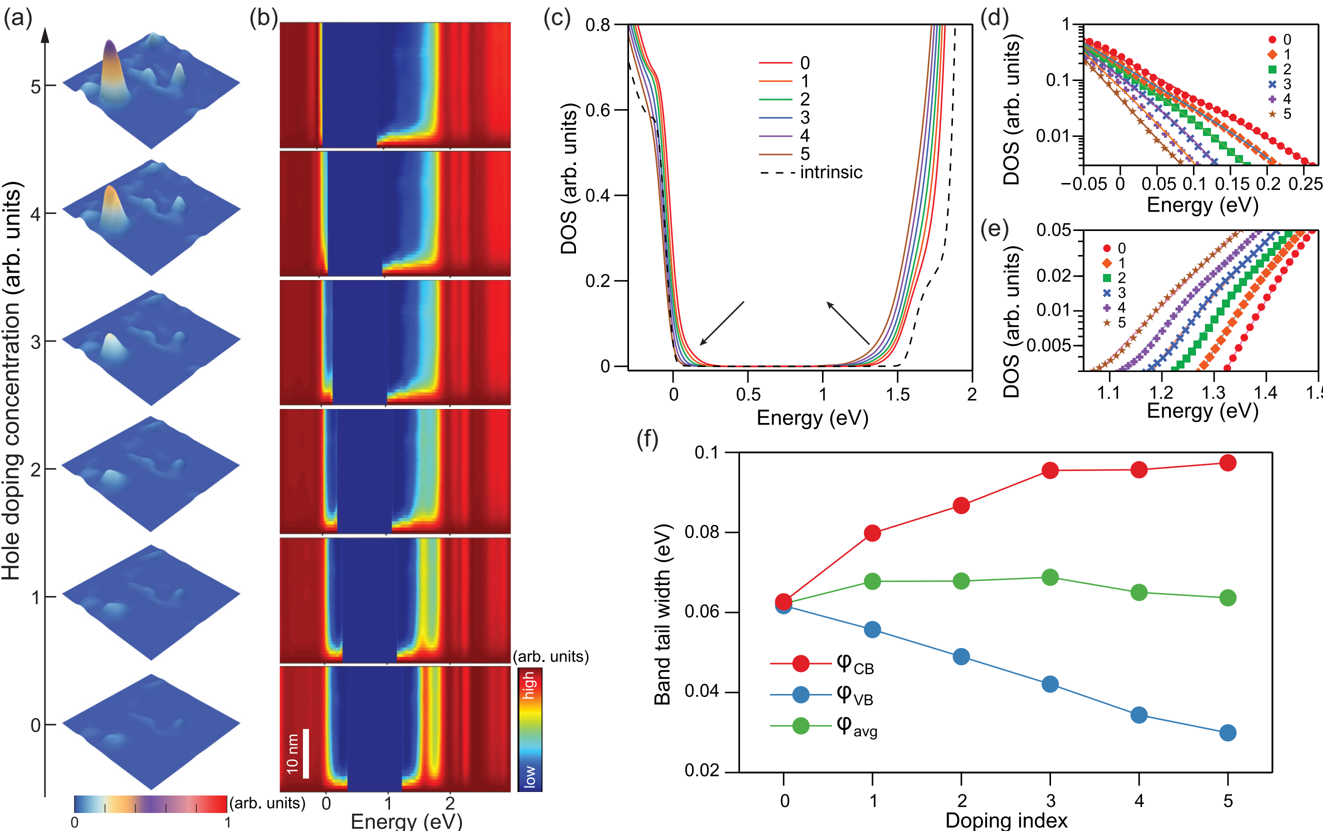

FIG. 7. Band edge flattening via hole doping in structural disorder. (a) Tight-binding calculations of doping charge densities in structurally disordered MoS_2 with various hole doping levels. Charge localization was correlated with curvature structures in MoS_2. The structural disorder corresponds to case 1 in Fig. 3. The 0 index indicates the intrinsic (neutral) case and the larger index means the higher doping level. (b) The radial-averaged autocorrelation profiles corresponding to (a). Rapidly decaying regions near the band edges characterize the band tail regions. The doping case 5 shows the flattening limit of the valence band edge. (c) The calculated DOS corresponding to (a). The arrows in the plot indicates widening of the conduction band tail and the flattening of the valence band edge through hole doping. [(d), (e)] Close-up log-plot of valence (d) and conduction (e) band tails in (c). (f) Plot of the band tail widths for the conduction (φ_{CB}) and valence (φ_{VB}) band sides, extracted from DOS results (c). The average (φ_{avg}) of the conduction and valence band tail widths is nearly constant regardless of the hole doping level.

The upper boundaries of the conduction band tail range from multifractal analysis in Fig. 6(d) are close to the critical energy of the localization-delocalization transition, satisfying the theoretical prediction for the criticality, $\eta = -\Delta_2 = \alpha_0 - 2$ [3,16]. This naturally results from band tails consisting of the localized states and the band tail boundaries meeting the extended states, as defined by the critical energy [36]. It is essential to mention that the critical energy differs from the mobility edge defined in a conventional rigid DOS case without band edge flattening.

The peak position α_0 of the singularity spectrum at the critical energy acts like an order parameter of $\alpha_0 - d$, where d is the dimension of the system (for 2D systems, $d = 2$) [24]. If α_0 is close to the system dimension of 2, the system approaches the metallic limit. As the electron (hole) doping level increases, the band edge flattening induces a uniform distribution of LDOS at an energy above (below) the critical energy. Indeed, the peak position α_0 of the singularity spectra of the uniform states over the critical energy is almost 2 (spatial dimension of the system) as shown in Fig. 6(d) (above 0 eV), approaching the metallic limit. At the limit of the band edge flattening through electron doping, the critical energy approaches the conduction band edge with vanishing of the conduction band tail region. The variation of α_0 larger than 2 reflects the localized states forming the band tails, originated from the structural disorder.

F. Critical doping concentration

Recognizing the parameters crucial for quantum criticality is foundational in understanding critical phenomena. In this context, we provide insight into how structural-disorder-driven MIT is dictated by the correlation between critical doping concentrations and structural disorder strength. As the doping-induced band edge flattening reduces the band tail range, the critical energy approaches the band edge. The presence of localized states triggered MIT in structurally disordered 2D semiconductors. The critical doping concentration regarding the Fermi level corresponds to the vanishing point of the conduction (valence) band tail along with the band edge flattening induced by electron (hole) doping. Therefore, the critical doping concentration depends on the degree of the structural disorder associated with the formation of band tails or localized states. If the ideally flat MoS_2 exists, the

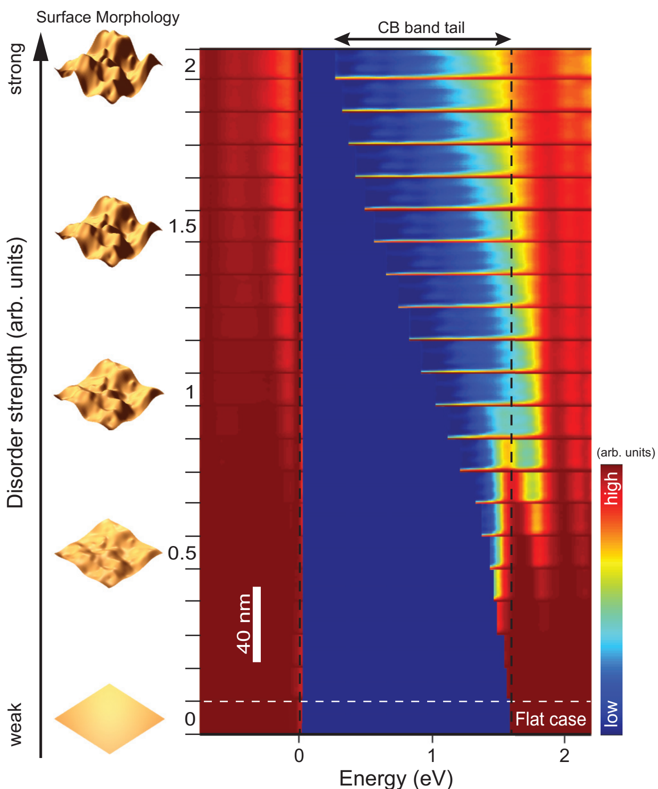

FIG. 8. Structural disorder effect for the valence band edge flattening via hole doping. The radial-averaged autocorrelation profiles as a function of structural disorder strengths, as the presented surface morphologies on the left. The tight-binding results show that flattening of the valence band edge through hole doping exhibited widening of the conduction band tail ranges which displayed rapid decaying in the radial-averaged autocorrelation.

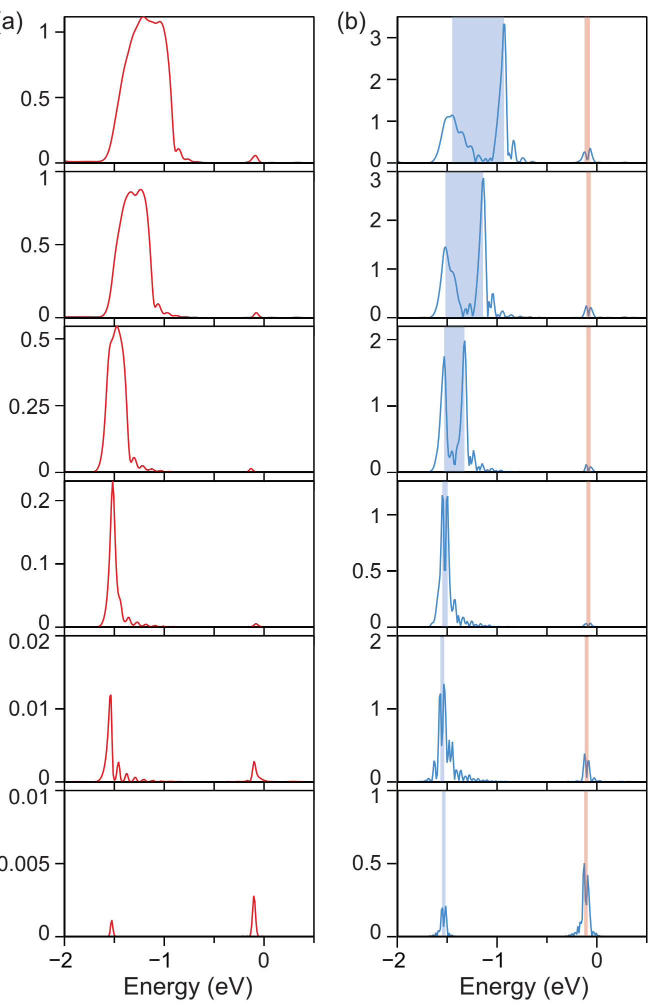

FIG. 9. Influence of structural disorder on α_0 amplitudes. (a) The amplitude of α_0 presents a sensitivity to structural disorder strength, particularly at the limit of band edge flattening. (b) The absolute value of the derivative of α_0. The range of band tails at the valence band edges scales with the structural disorder strength. Progressing from the bottom to the top, each row in both (a) and (b) aligns with the following average values of absolute bending strain: 0%, 0.253%, 0.507%, 0.761%, 1.015%, 1.268%, and 1.522%, in that order.

critical doping concentration at finite temperatures is related to the intrinsic carrier concentration. At 0 K, the intrinsic carrier concentration is expected to be zero. In a perfectly flat scenario, doping charge directly contributes to increased conductance. However, in a 2D semiconductor that is not flawlessly flat, the inherent curvature results in charge localization. This invariably gives rise to the metal-insulator transition, which should be detectable at very low temperatures even when the structural disorder is minimal. It is worth noting that in practical terms, 2D semiconductors are never perfectly flat due to a myriad of physical factors, including substrate surface roughness, trapping of atoms/molecules, and so on. The critical doping concentration was determined using tight-binding calculations for various structural disorder strengths (Fig. 3), and it is displayed in Fig. 6(i) together with the previous experimental result of MoS_2 on SiO_2. The average of absolute bending strain was obtained from the structural disorder. Stronger structural disorder induces a larger critical doping concentration, which originates from the capacity of the localized states. After filling the localized states, delocalized states start to be occupied. The experimental average value of absolute bending strain in MoS_2 on SiO_2 was $\sim$2% [20], and the critical doping concentration of MIT in MoS_2 on SiO_2 was reported as $\sim 1 \times 10^{13}$ cm^{-2} [9,11]. If the nonzero temperature is sufficient to activate the carrier excitations, the effective critical doping concentration becomes lower than the critical doping concentration at 0 K because thermally excited carriers aid conductivity (through percolation), as observed in the previous results [11].

III. SUMMARY AND CONCLUSIONS

In summary, we investigated the effect of structural disorder on the microscopic origin of MIT in 2D semiconductors using autocorrelation and multifractal analysis with experimental results and tight-binding calculations. The radial-averaged autocorrelation profiles and singularity spectra, as a function of the structural disorder strengths, with a doping-induced band edge flattening characterized band tails and critical behaviors of the localization-delocalization transition. The radial-averaged autocorrelation profiles characterized the localization/correlation lengths and ranges of

band tails through decaying behaviors. From the multifractal analysis of LDOS, we confirmed that the absolute value of first derivatives of their peak positions ($|d\alpha_0(E)/dE|$) characterized the band tail ranges. Along with the conduction (valence) band edge flattening through electron (hole) doping, the conduction (valence) band tail range shrank close to zero, and the critical energy approached the conduction (valence) band edge. Eventually, the divergence of localization length as a critical behavior occurred when the Fermi level crossed the critical energy by doping. The extended states above the critical energy exhibited uniformity with the band edge flattening, regardless of the structural disorder. The $\alpha_0 - 2$ acts like an order parameter that realizes the localized and extended states along with the band edge flattening through doping. We found that the critical doping concentration for MIT at 0 K is correlated with the strength of structural disorder. At the finite temperatures (not 0 K), thermal excitation of the carriers resulted in percolation-type MIT, which shows an effective doping concentration below the critical doping concentration at 0 K. We believe that the understanding of the curvature-induced charge localization, band tails, and the localization-delocalization transition or MIT in structurally disordered 2D semiconductors leads to the fundamental concepts of quantum phase transitions and criticality for unique quantum electronic/optoelectronic device applications.

ACKNOWLEDGMENTS

J.-H.P. and J.K. acknowledge the support from the U.S. Army Research Office (ARO) MURI project under Grant No. W911NF-18-1-04320431 and the U.S. Army Research Office through the Institute for Soldier Nanotechnologies at MIT, under Cooperative Agreement No. W911NF-18-2-0048.

APPENDIX A: BAND EDGE FLATTENING VIA HOLE DOPING

Following the same mechanism as explained for the conduction band edge flattening via electron doping, the valence band edge flattening via hole doping is triggered by the localization of holes in the curvature-induced valence band edge (or band gap) fluctuations. The main differences from the electron doping cases [Figs. 4 and 5] are the sign of the charge in the Coulomb interaction and the capacity of the density of states near the band edge. Figure 7 shows the localization of holes, band tail formation, and characteristic band tail width as a function of hole doping concentration.

APPENDIX B: STRUCTURAL DISORDER EFFECT FOR THE BAND EDGE FLATTENING VIA HOLE DOPING

The strength of structural disorder determines the capacity of charge localization through curvature-induced band edge (or band gap) fluctuations. At the limit of the valence band edge flattening, the conduction band tail is stretched with the structural disorder strength [Fig. 8], which is similar to the electron doping cases [Fig. 4(c)].

APPENDIX C: SINGULARITY SPECTRUM OF LDOS (STS) MAP

For the multifractal analysis, we followed the methods of Chhabra and Jensen [37]. The singularity spectrum $f(\alpha)$ is the fractal dimension of spatial domains that the amplitude of electron wave functions ψ at a position $\boldsymbol{r}$ follows $|\psi(\boldsymbol{r})|^2 \sim L^{-\alpha}$, where L is the (effective) linear size of the system [3,24,37]. The probability of finding electrons from $|\psi(\boldsymbol{r})|^2$ with moment q in a box of linear size l_b is given by

$$P_i^q(l_b) = \sum_{j \in \text{box}_i(l_b)} |\psi(\boldsymbol{r}_j)|^{2q}, \tag{C1}$$

where the system domain is divided by boxes of linear size l_b [$\text{box}_i(l_b)$]. The normalized population measure of moment q is defined by

$$\mu_i(q, l_b) = P_i^q(l_b) / \sum_j P_j^q(l_b). \tag{C2}$$

A singularity strength α_i is defined to satisfy that $P_i^q(l_b) \propto \lambda^{-\alpha_i}$, where λ is the normalized spatial measure defined by l_b/L. The population count $N(\alpha_i)$ is the number of boxes for the singularity strength α_i, where α_i is in between α and $\alpha + d\alpha$. The singularity spectrum $f(\alpha)$ is introduced by $N(\alpha) \propto \lambda^{-f(\alpha)}$, which indicates the fractal dimension of the $N(\alpha)$ box domains.

The singularity spectrum $f[\alpha(q)]$ and average of the singularity strength $\alpha(q)$ are defined by

$$f[\alpha(q)] = \lim_{\lambda \to 0} \frac{1}{\ln \lambda} \sum_i^{N_t} \mu_i(q, l_b) \ln \mu_i(q, l_b), \tag{C3}$$

$$\alpha(q) = \lim_{\lambda \to 0} \frac{1}{\ln \lambda} \sum_i^{N_t} \mu_i(q, l_b) \ln P_i(l_b). \tag{C4}$$

where N_t is the total number of boxes of $(l_b/L)^{-\mathrm{d}}$ (d is the system dimension.).

APPENDIX D: TIGHT-BINDING METHOD FOR STRUCTURAL DISORDER

The tight-binding method with the three-band model of transition metal dichalcogenides [25] was applied to calculate the random fluctuations of local surface height in monolayer MoS_2. Structural disorder for structural modeling was generated by the superposition of random Gaussian bumps for height fluctuations within the elastic limit of MoS_2. The disorder strength was scaled by control of the surface fluctuation range. The unit cell size was $25 \times 25\,\text{nm}^2$ and a periodic boundary condition was applied to avoid a boundary effect. The randomly deformed structural models within third-nearest neighbor were calculated to obtain LDOS of each d orbital (d_{z^2}, d_{xy}, and $d_{x^2-y^2}$). The changes of hopping parameters t_{ij} between i and j sites by strain were considered as

$$t_{ij} = t_{ij}^0 \exp\left(-\beta\left[\frac{a_{ij}}{a_0} - 1\right]\right), \tag{D1}$$

where a_0, t_{ij}^0, and a_{ij} are unstrained lattice distance, primitive hopping parameter, and strained distance between i and j sites, respectively. The factor β was chosen as 5, empirically.

APPENDIX E: DENSITY FUNCTIONAL THEORY CALCULATIONS FOR BAND EDGE FLATTENING

The first-principles calculations were performed to investigate the curvature-induced band gap fluctuations and doping-induced band edge flattening, using the Vienna *ab initio* simulation package (VASP) based on the density functional theory with a plane-wave basis set [38]. The pseudopotentials in the projector augmented wave (PAW) formalism with the Perdew-Burke-Ernzerhof (PBE) parametrization of the general gradient approximation (GGA) were used as implemented in VASP [39,40]. The spherical bending structure of a Gaussian shape was modeled by a slab geometry with a vacuum of ∼14 Å. The structural model with a Gaussian shape was fully relaxed until the residual forces of each atom were less than 0.02 eV/Å. The plane-wave cutoff energy was 400 eV. The Γ point was used for the surface Brillouin zone integration due to the largeness of the unit cell ($47.4 \times 43.79\,\text{nm}^2$) with a heavy computational load. The energy convergence was achieved with a tolerance of 10^{-6} eV.

APPENDIX F: SYNTHESIS OF MoS_2 MONOLAYERS

Monolayer MoS_2 film was grown under low pressure by metal-organic chemical vapor deposition (MOCVD) [41]. Molybdenum hexacarbonyl [$Mo(CO)_6$, Sigma-Aldrich] and diethyl sulfide ($(C_2H_5)_2S$, Sigma Aldrich) were selected as precursors of Mo and S, respectively, and were supplied in a gas phase into a 1-in. quartz tube furnace by the help of a bubbler system with Ar as a carrier gas. The MoS_2 film was synthesized on a 300-nm-thick SiO_2/Si wafer with the flow rate of 100 SCCM (standard cubic centimeter per minute) for Ar, 0.6 SCCM for $Mo(CO)_6$, and 2.0 SCCM for $(C_2H_5)_2S$ under a growth temperature below 350 °C and a growth time of 15 h. After growth, the furnace heat was turned down until it reached room temperature.

APPENDIX G: CRITICAL DOPING CONCENTRATION

The critical doping concentration was determined through the complete occupancy of localized states until the threshold of band edge flattening via doping was reached. Once this threshold is met, there are not any favored sites for the doping charge to localize, causing the doping charge to transition into free carriers beyond the critical doping concentration. The critical doping charge concentration was determined by the integration of the density of states over the energy ranges of localized states (band tails) at the limit of band edge flattening. The absolute values of the critical doping concentrations were calibrated by DFT-calculated Fermi levels and experimental results from Ref. [9].

APPENDIX H: STRUCTURAL DISORDER EFFECT AT THE CONDUCTION BAND EDGE FLATTENING LIMIT

The amplitude of α_0 from the multifractal analysis is dependent on both the strength of the structural disorder and the flattening of band edges through doping. When an LDOS map at a given energy is more homogeneous, the amplitude of α_0 becomes closer to 2 as the metallic limit in a 2D system. The sensitivity of α_0 to structural disorder at the conduction band edge flattening limit is shown in Fig. 9(a). The absolute value of the derivative of α_0, which is less sensitive to the structural disorder, characterizes the band tail ranges [Fig. 9(b)].

[1] V. Dobrosavljević, N. Trivedi, and J. M. Valles, Jr., *Conductor-Insulator Quantum Phase Transitions* (Oxford University Press, Oxford, 2012).

[2] E. Abrahams, *50 Years of Anderson Localization* (World Scientific, Singapore, 2010).

[3] F. Evers and A. D. Mirlin, Anderson transitions, Rev. Mod. Phys. **80**, 1355 (2008).

[4] P. W. Anderson, Absence of diffusion in certain random lattices, Phys. Rev. **109**, 1492 (1958).

[5] E. Abrahams, P. W. Anderson, D. C. Licciardello, and T. V. Ramakrishnan, Scaling of localization: Absence of quantum diffusion in two dimensions, Phys. Rev. Lett. **42**, 673 (1979).

[6] S. V. Kravchenko, G. V. Kravchenko, J. E. Furneaux, V. M. Pudalov, and M. D'Iorio, Possible metal-insulator transition at $B = 0$ in two dimensions, Phys. Rev. B **50**, 8039 (1994).

[7] E. Abrahams, S. V. Kravchenko, and M. P. Sarachik, Metallic behavior and related phenomena in two dimensions, Rev. Mod. Phys. **73**, 251 (2001).

[8] B. Spivak, S. V. Kravchenko, S. A. Kivelson, and X. P. A. Gao, Transport in strongly correlated two dimensional electron fluids, Rev. Mod. Phys. **82**, 1743 (2010).

[9] B. Radisavljevic and A. Kis, Mobility engineering and metal-insulator transition in monolayer MoS_2, Nat. Mater. **12**, 815 (2013).

[10] Z. Yu, Z.-Y. Ong, S. Li, J.-B. Xu, G. Zhang, Y.-W. Zhang, Y. Shi, and X. Wang, Analyzing the carrier mobility in transition-metal dichalcogenide MoS_2 field-effect transistors, Adv. Funct. Mater. **27**, 1604093 (2017).

[11] X. Chen, Z. Wu, S. Xu, L. Wang, R. Huang, Y. Han, W. Ye, W. Xiong, T. Han, G. Long, Y. Wang, Y. He, Y. Cai, P. Sheng, and N. Wang, Probing the electron states and metal-insulator transition mechanisms in molybdenum disulphide vertical heterostructures, Nat. Commun. **6**, 6088 (2015).

[12] A. Punnoose and A. M. Finkel'stein, Metal-insulator transition in disordered two-dimensional electron systems, Science **310**, 289 (2005).

[13] V. Dobrosavljević, E. Abrahams, E. Miranda, and S. Chakravarty, Scaling theory of two-dimensional metal-insulator transitions, Phys. Rev. Lett. **79**, 455 (1997).

[14] A. Georges, G. Kotliar, W. Krauth, and M. J. Rozenberg, Dynamical mean-field theory of strongly correlated fermion systems and the limit of infinite dimensions, Rev. Mod. Phys. **68**, 13 (1996).

[15] A. D. Mirlin and F. Evers, Multifractality and critical fluctuations at the Anderson transition, Phys. Rev. B **62**, 7920 (2000).

[16] I. S. Burmistrov, I. V. Gornyi, and A. D. Mirlin, Multifractality at Anderson transition with Coulomb interaction, Phys. Rev. Lett. **111**, 066601 (2013).

[17] E. Cuevas and V. E. Kravtsov, Two-eigenfunction correlation in a multifractal metal and insulator, Phys. Rev. B **76**, 235119 (2007).

[18] A. D. Mirlin and Y. V. Fyodorov, Distribution of local densities of states, order parameter function, and critical behavior near the Anderson transition, Phys. Rev. Lett. **72**, 526 (1994).
[19] B. G. Shin, J.-H. Park, J.-Y. Juo, J. Kong, and S. J. Jung, Structural-disorder-driven critical quantum fluctuation and localization in two-dimensional semiconductors, Nat. Commun. **14**, 2283 (2023).
[20] B. G. Shin, G. H. Han, S. J. Yun, H. M. Oh, J. J. Bae, Y. J. Song, C.-Y. Park, and Y. H. Lee, Indirect bandgap puddles in monolayer MoS_2 by substrate-induced local strain, Adv. Mater. **28**, 9378 (2016).
[21] S. Deng, E. Gao, Z. Xu, and V. Berry, Adhesion energy of MoS_2 thin films on silicon-based substrates determined via the attributes of a single MoS_2 wrinkle, ACS Appl. Mater. Interfaces **9**, 7812 (2017).
[22] R. I. González, F. J. Valencia, J. Rogan, J. A. Valdivia, J. Sofo, M. Kiwi, and F. Munoz, Bending energy of 2D materials: Graphene, MoS_2 and imogolite, RSC Adv. **8**, 4577 (2018).
[23] Y. Lin, X. Ling, L. Yu, S. Huang, A. L. Hsu, Y.-H. Lee, J. Kong, M. S. Dresselhaus, and T. Palacios, Dielectric screening of excitons and trions in single-layer MoS_2, Nano Lett. **14**, 5569 (2014).
[24] M. Janssen, Multifractal analysis of broadly-distributed observables at criticality, Int. J. Mod. Phys. B **8**, 943 (1994).
[25] G.-B. Liu, W.-Y. Shan, Y. Yao, W. Yao, and D. Xiao, Three-band tight-binding model for monolayers of group-VIB transition metal dichalcogenides, Phys. Rev. B **89**, 039901 (2014).
[26] H. M. Cohen, M. Y. Chou, E. N. Economou, S. John, and C. M. Soukoulis, Band tails, path integrals, instantons, polarons, and all that, IBM J. Res. Dev. **32**, 82 (1988).
[27] W. Zhu, T. Low, Y.-H. Lee, H. Wang, D. B. Farmer, J. Kong, F. Xia, and P. Avouris, Electronic transport and device prospects of monolayer molybdenum disulphide grown by chemical vapour deposition, Nat. Commun. **5**, 3087 (2014).
[28] K. Hsieh, V. Kochat, X. Zhang, Y. Gong, C. S. Tiwary, P. M. Ajayan, and A. Ghosh, Effect of carrier localization on electrical transport and noise at individual grain boundaries in monolayer MoS_2, Nano Lett. **17**, 5452 (2017).
[29] Y. Asada, K. Slevin, and T. Ohtsuki, Numerical estimation of the β function in two-dimensional systems with spin-orbit coupling, Phys. Rev. B **70**, 035115 (2004).
[30] R. Sepehrinia, Universality of Anderson transition in two-dimensional systems of symplectic symmetry class, Phys. Rev. B **81**, 045104 (2010).
[31] Y. Su and X. R. Wang, Role of spin degrees of freedom in Anderson localization of two-dimensional particle gases with random spin-orbit interactions, Phys. Rev. B **98**, 224204 (2018).
[32] H. Ochoa, R. Zarzuela, and Y. Tserkovnyak, Emergent gauge field from curvature in single layers of transition-metal dichalcogenides, Phys. Rev. Lett. **118**, 026801 (2017).
[33] H. Duan, P. Guo, C. Wang, H. Tan, W. Hu, W. Yan, C. Ma, L. Cai, L. Song, W. Zhang, Z. Sun, L. Wang, W. Zhao, Y. Yin, X. Li, and S. Wei, Beating the exclusion rule against the coexistence of robust luminescence and ferromagnetism in chalcogenide monolayers, Nat. Commun. **10**, 1584 (2019).
[34] Z. Guguchia, A. Kerelsky, D. Edelberg, S. Banerjee, F. von Rohr, D. Scullion, M. Augustin, M. Scully, D. A. Rhodes, Z. Shermadini, H. Luetkens, A. Shengelaya, C. Baines, E. Morenzoni, A. Amato, J. C. Hone, R. Khasanov, S. J. L. Billinge, E. Santos, A. N. Pasupathy *et al.*, Magnetism in semiconducting molybdenum dichalcogenides, Sci. Adv. **4**, eaat3672 (2018).
[35] Y. Su, C. Wang, Y. Avishai, Y. Meir, and X. R. Wang, Absence of localization in disordered two-dimensional electron gas at weak magnetic field and strong spin-orbit coupling, Sci. Rep. **6**, 33304 (2016).
[36] M. H. Cohen, C. M. Soukoulis, and E. N. Economou, Interband optical absorption in amorphous semiconductors, in Optical Effects in Amorphous Semiconductors, AIP Conf. Proc. No. 120 (AIP, Melville, NY, 1984), p. 371.
[37] A. Chhabra and R. V. Jensen, Direct determination of the $f(\alpha)$ singularity spectrum, Phys. Rev. Lett. **62**, 1327 (1989).
[38] G. Kresse and J. Furthmüller, Efficiency of *ab-initio* total energy calculations for metals and semiconductors using a plane-wave basis set, Comput. MatER. Sci. **6**, 15 (1996).
[39] J. P. Perdew, K. Burke, and M. Ernzerhof, Generalized gradient approximation made simple, Phys. Rev. Lett. **77**, 3865 (1996).
[40] G. Kresse and J. Joubert, From ultrasoft pseudopotentials to the projector augmented-wave method, Phys. Rev. B **59**, 1758. (1999).
[41] J.-H. Park, A.-Y. Lu, P.-C. Shen, B. G. Shin, H. Wang, N. Mao, R. Xu, S. J. Jung, D. Ham, K. Kern, Y. Han, and J. Kong, Synthesis of high-performance monolayer molybdenum disulfide at low temperature, Small Methods **5**, 2000720 (2021).